Epithelium Stratifies via Nucleation and Growth Induced by Foam-Geometric Instability

Shuya Fukamachi[1], Razib Datta[1], Duligengaowa Wuergezhen[2], Takehiko Ichikawa[3], Rei Yagasaki[3], Shuhei A. Horiguchi[3], Phoebe Leeaw[1], Kohei Omachi[2], Aiko Sada[4], Itaru Imayoshi[5,6], Kentaro Kajiwara[7], Tetsuya Hiraiwa[8], Masanobu Oshima[3,9], Takeshi Fukuma[3], Hironobu Fujiwara[2], Satoru Okuda[3,10*]

[1] Graduate School of Frontier Science Initiative, Kanazawa University, Kanazawa 920-1192, Japan

[2] Laboratory for Tissue Microenvironment, RIKEN Center for Biosystems Dynamics Research (BDR), Kobe 650-0047, Japan

[3] Nano Life Science Institute, Kanazawa University, Kanazawa 920-1192, Japan

[4] Division of Skin Regeneration and Aging, Medical Institute of Bioregulation, Kyushu University, Fukuoka 812-8582, Japan

[5] Graduate School of Biostudies, Kyoto University, Kyoto 606-8501, Japan

[6] Institute for Life and Medical Sciences, Kyoto University, Kyoto 606-8501, Japan

[7] Research Institute for Microbial Diseases, Osaka University, Osaka 565-0871, Japan

[8] Institute of Physics, Academia Sinica, Taiwan 115201, Taiwan

[9] Cancer Research Institute, Kanazawa University, Kanazawa 920-1192, Japan

[10] Sapiens Life Sciences, Evolution and Medicine Research Center, Kanazawa 920-1192, Japan

[*] Corresponding author: satokuda@staff.kanazawa-u.ac.jp (S.O.)

Abstract

The epithelium undergoes stratification, transitioning from a monolayer to a multilayer structure, across broad phenomena. Recent studies have identified several cell behaviors as triggers, including junctional tension, cell density and geometry, and topological defects. However, how these factors drive stratification throughout the entire epithelium remains poorly understood. Here, we report a mechanism underlying epithelial stratification that mirrors the physics of phase transition. Combining cell culture with three-dimensional vertex modeling, we demonstrate that epithelium stratifies via nucleation-growth process, i.e., multilayer origins dispersedly appear and expand across the epithelium via unordered intermediate states. This process is akin to a phase transition induced by a mechanical instability inherent in the foam-like geometry of the epithelium. Moreover, this concept applies to embryonic skin development and malignant transformation of cancer. These findings conceptualize epithelial stratification as a form of a phase transition governed by nucleation and growth, offering a physical perspective on various epithelial developments.

Keywords

Collective motion, phase transition, nucleation and growth, mechanical instability, tissue mechanics, epithelial morphogenesis, foam physics, vertex model, skin development, cancer progression

Introduction

Many epithelia develop multilayer sheet structures[1], such as those found in the skin[2], hair follicles[3], cornea[4], esophagus[5], stomach[6], intestine[7], bronchus[8], and brain[9]. These multilayer structures typically evolve from a monolayer through a stratification process, a key phenomenon in embryogenesis. Defects in this process lead to fatal diseases. For instance, mouse skin, which is normally multilayered during embryogenesis, remains a monolayer when the p63 gene is defective, resulting in postnatal death due to dehydration[10–12]. In tumorigenesis, abnormal cells stratify to form tumors on epithelial sheets[13]. Consequently, epithelial stratification has been extensively investigated in various biological contexts. However, although key molecules and cell behaviors have been clarified, the mechanism of collective cell dynamics leading to stratification of the entire epithelium remains unclear. Thus, a significant need exists to develop a comprehensive understanding of the stratification process, particularly how individual cell delaminations integrate into overall stratification.

During epithelial stratification, cells typically delaminate from either the apical or basal side and accumulate vertically within the sheet. Several mechanisms have been proposed for delamination of individual cells. For example, in skin and brain development, cell delamination often results directly from vertically oriented cell divisions[14–16], whereas recent pioneering work has shown that cells stratify even without the regulation of cell division orientation[15]. Additionally, cells that lose their basal side during mitosis can regain it by elongating their protrusions[17,18]. These findings suggest that transient vertical arrangements by oriented cell divisions may not be sufficient; rather, a balance of mechanical forces among cells is required to form a stable, stratified structure.

From a physical viewpoint, apical junctional forces, such as heightened actomyosin contractility and reduced cadherin-mediated adhesion, are well-known contributors to cell delamination[19–24]. Moreover, an increase in cell density within the epithelial plane can drive cells out of layers[25–27]. Recent studies have also revealed the impact of cell geometry on this process[28–30]; particularly, topological defects trigger initiation of the stratification process[31,32]. These findings underscore the critical role of mechanical forces in epithelial stratification. However, current understanding is largely limited to the initiation of the stratification process, i.e., single-cell delamination, and little is known about how the delamination of individual cells expands into overall tissue stratification. Specifically, it is unknown whether this transition propagates as a wave originating from a specific point of cell delamination or instead emerges from numerous origins, spreading through an unordered intermediate state, and what physics underlies this transition.

To bridge the gap from cell- to tissue-scale mechanics, we combined three-dimensional (3D) quantifications and multicellular dynamics modeling. This approach elucidates how individual cells

mechanically control the overall layer structure of the epithelium. Two primary requirements guided our study. First, we aimed to observe the collective cell dynamics in 3D space during epithelial stratification. Although the kinetic behaviors of individual cell delamination are well documented, the collective motions of cells throughout the entire stratification process remain largely unexplored. Specifically, the spatial distribution of delaminated cells during stratification and their subsequent influence on the delamination of other cells requires further clarification. Second, we focused on understanding the physical mechanisms underlying collective cell motion during stratification. Given the challenges of monitoring mechanical interactions in 3D tissue structures, we developed a 3D vertex model[33,34]. This model captures the dynamics of stratification, including 3D deformation and cellular arrangements. This approach allows for a comprehensive analysis of the 3D structures and mechanics involved in multicellular arrangements during epithelial stratification.

To elucidate the fundamental mechanisms of epithelial stratification, we observed the stratification process of Madin-Darby canine kidney (MDCK) cells cultured on a dish and employed a 3D vertex model to understand the physical mechanisms of stratification. Although MDCK cell cultures and vertex models have often been used to study cell delamination[35–37], our work is the first trial to extensively apply them to stratification. In both systems, we recapitulated the kinetic process of epithelial stratification at single-cell resolution, i.e., how individual cells delaminate and accumulate to form multilayer structures. To analyze this process, we quantified 3D cell configurations and their dynamics to reveal the physical concept of the phase transition with nucleation and growth, which could apply to epithelial stratification. To understand the mechanisms of delamination, we performed analytical calculations using a 3D vertex model to reveal a mechanical instability inherent in the foam-like epithelial geometry. To clarify the model predictions, we further conducted image analyses and atomic force microscopy (AFM) measurements. Finally, we explored the applicability of the nucleation-growth concept to embryogenesis and carcinogenesis by observing skin development in mouse embryos and malignant transformation of cancer using intestinal organoids. Throughout these interdisciplinary investigations, we conceptualized epithelial stratification based on the physics of phase transitions.

Results

Epithelial stratification is akin to a phase transition with nucleation and growth

To understand the kinetic process of epithelial stratification, we employed a simple MDCK cell culture on a dish coated with collagen gel (Fig. 1**a**, see Materials and Methods). The cells spread and stratified on the gel, and we identified four distinct stages during this stratification (Fig. 1**b**): a nonconfluent structure where cells partially occupied the dish, a complete monolayer with cells densely packed on the dish, a mixed layer featuring partially stratified cells, and a multilayer with cells mostly stratified. Throughout the stratification, the tight junction marker ZO1 consistently localized at the cell-cell boundaries around the apical surface of the entire sheet (Fig. 1**b**). In contrast, cells delaminating from the apical side lost their junctions. Thus, cells stratified from a monolayer to a multilayer structure while maintaining the apicobasal polarity of the entire tissue.

To understand this stratification process, we quantified its time evolution (detailed in Materials and Methods) by introducing the stratification ratio, ξ, defined as the occupancy ratio of the stratified domain on the plane of the dish:

$$\xi = 1 - \frac{N_{\mathrm{ab}}}{N_{\mathrm{t}}}. \tag{1}$$

In Eq. 1, N_{ab} represents the number of cells with both apical and basal surfaces, and N_{t} indicates the total number of cells. We noted a gradual increase in ξ from 0 to approximately 1, with an S-shaped curve (Fig. 1**c**,**d**), signifying a structural crossover from a complete monolayer to a fully multilayer arrangement. We further calculated the radial distributions of nuclear centroids (detailed in Materials and Methods) and found that the distances between proximal cells were regular, whereas the distances between distal cells were disorganized (Fig. 1**e**), showing that epithelia maintain amorphous-like structures during stratification.

Next, to understand the kinetic process of individual cell behaviors, we examined their delamination processes. During stratification, individual cells gradually delaminate by losing their apical or basal side, dividing the entire epithelium into two domains: monolayer or multilayer. We identified two characteristic events in stratification: nucleation, where cell delaminations occur individually in a monolayer domain (Fig. 1**f**), and growth, where cell delaminations occur at the boundary of the monolayer adjacent to a multilayer domain (Fig. 1**g**). These events mirror the physical processes of nucleation and growth often observed in structural phase transitions such as crystallization.

To understand the time evolution of the nucleation and growth events in epithelial stratification, we quantified their frequencies. Because it was difficult to directly measure each event, we counted the number of delaminated cells, categorizing them as either dispersed or clustered, i.e., isolated or

adjacent to other delaminated cells (detailed in Materials and Methods). Dispersed delaminations initially increased during the early stage of stratification, which was later followed by an increase in the number of adjacent delaminations (Fig. 1**h**). Consistently, the most frequent size of delaminated cell clusters shifted from single cells to multiple cells (Fig. 1**i**). Notably, the adjacent delamination count eventually surpassed that of dispersed delaminations. This pattern is reminiscent of the nucleation-growth process of structural phase transitions, characterized by initial frequent nucleation and subsequent nuclear growth. This similarity draws an analogy between the mechanisms of epithelial stratification and the phase transition governed by nucleation and growth.

Based on the analogy between epithelial stratification and nucleation-growth physics, we applied methods used in the physical understanding of nucleation and growth to investigate the epithelial stratification process. Specifically, we applied the well-known Johnson-Mehl-Avrami-Kohnogorov (JMAK) model[38] and fitted the time evolution of ξ. Originating from a classical nucleation-growth theory, the JMAK model describes the progression of nucleation and growth and is expressed as a simple sigmoid function representing the time variation of the phase proportion:

$$\xi(t) = 1 - \exp[-k(t - t_0)^{\nu}]. \tag{2}$$

In Eq. 2, k represents the phase growth rate, t_0 represents the initiation time, and ν represents the Avrami exponent. Remarkably, ξ values from the MDCK cell culture were successfully fitted using the JMAK model (Fig. 1**c**,**d**; detailed in Materials and Methods). The Avrami exponent was determined as $\nu = 2.29$. Generally, ν reflects the property of the phase transition, and it is equal to 3 in the ideal case of two-dimensional (2D) growth with random nucleation sites. However, ν is decreased if the nucleation site distribution is not random, indicating restricted growth. Our obtained ν value is reasonable, justifying the application of the JMAK model, and lower than 3, suggesting that nucleation is influenced by the already stratified domain. These results demonstrate that epithelial stratification can be conceptualized as a form of nucleation-growth process.

3D foam mechanics-based modeling reproduces epithelial stratification

To address nucleation-growth mechanisms underlying epithelial stratification, we assumed that epithelial stratification can be regarded as a mechanical process of foam-like materials, and we developed a 3D vertex model to investigate its mechanisms (detailed in Materials and Methods). This model overcomes the limitations of conventional models; while 3D particle models and 2D vertex models have unveiled the mechanics of stratification[13,39–41], they have limitations in describing 3D cell deformations and arrangements. Our model describes a 3D foam geometry of the epithelium equilibrated under stress-free boundary conditions, assuming balanced mechanical forces among cells

(Fig. 2**a**, detailed in Materials and Methods). Cells have apicobasal polarity (Fig. 2**b**); based on observations of the tight junction marker ZO1 (Fig. 1**b**), we postulated that all cell-cell boundary surfaces comprised parts of the basolateral surfaces, and the other cell surfaces composing the tissue surface were defined as the apical surfaces. Moreover, we introduced two types of junctional contractility, which is well-known as a regulator of cell delamination: apical perimeter elasticity of each cell, Γ, and line tension at apical junctions, λ (Fig. 2**c**), which are well established to describe apical behaviors of epithelial cells in 2D space[42] and have been applied to those in 3D space[43–45]. While Γ harmonizes the size of apical cell surfaces across adjacent cells, λ works oppositely[30].

The mechanical behavior of cells with apicobasal polarity is represented by the effective energy U, expressed as

$$U = \sum_{\alpha}^{\text{cell}} \frac{K}{2}\left(\frac{V_\alpha}{V_0} - 1\right)^2 + \sum_{\alpha}^{\text{cell}} \kappa A_\alpha + \sum_{\alpha}^{\text{cell}} \Gamma (P_\alpha)^2 + \sum_{(\alpha\beta)}^{\text{junction}} \lambda l_{(\alpha\beta)} \,. \tag{3}$$

In Eq. 3, K, V_0, κ, Γ, and λ are constants, and $K, V_0, \kappa,$ and Γ are positive. α and β denote cell indices, and $(\alpha\beta)$ indicates a pair of the α-th and β-th cells. The first term represents the volume elastic energy, which restores the volume of each cell to V_0 with an elastic constant K. The second term is the basolateral surface energy, characterized by the surface tension, κ. The third term denotes the elastic energy of the apical junctional perimeter, contracted by an elastic constant, Γ. The fourth term accounts for the tensile energy at the junction between neighboring cells on the apical side, with the tension constant λ. Using this model, we numerically calculated the energy relaxation process from an initial condition of a complete monolayer (Fig. 2**a**, detailed in Materials and Methods) and obtained an equilibrium structure at the local energy minimum. During this relaxation, cell configurations were rearranged in 3D space, causing stratification. This cell rearrangement is described by introducing [H]-[I] operations (Fig. 2**d**), as suggested in a previous study[33], which describe the cell extrusion from a monolayer to either the apical or basal side (Fig. 2**d**-I), cell rearrangement in the plane of an epithelial sheet (Fig. 2**d**-II), and the collapse of the epithelial sheet, creating a hole (Fig. 2**d**-III).

By exploring the apical junctional parameters Γ and λ, we replicated all four epithelial structure types: nonconfluent structure (Fig. 2**e**), complete monolayer (Fig. 2**f**), mixed layer (Fig. 2**g**), and multilayer (Fig. 2**h**), corresponding to those observed in MDCK cell culture (Fig. 1**b**). We calculated the average number of layers in individual epithelia, which increased with Γ and λ (Fig. 2**i**). Moreover, we calculated the radial distribution functions (RDFs) of cell centroids (Fig. 2**j**) and found that the distances between proximal cells were regular. However, the distances between distal cells were disorganized, showing that epithelia maintain amorphous-like structures before and after stratification, corresponding to those observed in MDCK cell culture (Fig. 1**e**). These results demonstrate that our

model successfully recapitulated the amorphous-like epithelium structures and their transitions. Note that the regularity of the RDF was higher in the simulation than in the experiment. This could be because the volume of individual cells was set uniformly in the simulation, whereas it varied widely in the experiment.

To analyze the dependence of the layer structure on the apical junctional parameters Γ and λ, we calculated the stratification ratio, ξ (Fig. 2**k**). Under extremely small Γ and λ, the epithelium formed an incomplete monolayer, transitioning to a complete monolayer with a slightly larger Γ and λ. It transitioned from a complete monolayer to a mixed monolayer as Γ increased and to a complete multilayer structure as λ increased. Quantitatively, ξ jumped from 0 to 1 with an increase in λ in a switch-like manner (Fig. 2**l**), indicating a phase transition from monolayer to multilayer. Moreover, to understand the phase transition characteristics, we varied Γ and λ using the initial condition of a multilayer structure (Fig. 2**m**). The monolayer-to-multilayer transition was observed when using the initial condition of a monolayer (Fig. 2**m**, from points I to II), but the multilayer-to-monolayer transition did not occur when using a multilayer initial condition (Fig. 2**m**, from points II to III). These results show that although Γ and λ were set to values that maintained the monolayer when the simulation was performed with a monolayer as the initial condition, the epithelial structure could not return to the monolayer once it formed a multilayer structure. Thus, our 3D foam-based model replicates the monolayer-to-multilayer transition observed in epithelial stratification, characterizing it as a first-order-like phase transition.

Stratified domain growth determines either monolayer or multilayer phase

To understand the physical process of epithelial stratification, we observed the cell dynamics in the numerical simulations shown in Fig. 2. We identified both nucleation (Fig. 3**a**) and growth (Fig. 3**b**) events, as observed in MDCK cell culture (Fig. 1**f**,**g**). These alignments between the simulations and experiments suggest that our model successfully recapitulates the kinetic process of epithelial stratification at single-cell resolution.

To delve deeper into the nucleation-growth process, we calculated their ratios, denoted by f_{n} and f_{g}, respectively (detailed in Materials and Methods), and examined their dependencies on apical contractility: Γ and λ. Both f_{n} and f_{g} increased with Γ and λ (Fig. 3**c**,**d**). Importantly, f_{n} along did not distinguish between monolayer and multilayer structures: a monolayer formed at low f_{n} ($\lesssim 0.06$) when $\Gamma < 0.04$, while a multilayer structure formed at high f_{n} ($\gtrsim 0.02$) when $\Gamma > 0.04$ (Fig. 3**c**). In contrast, f_{g} differentiated these structures: monolayer and multilayer domains corresponded to lower ($\lesssim 0.1$) and higher ($\gtrsim 0.8$) f_{g} values across the entire range of Γ (Fig. 3**d**). Moreover, we examined

stratification processes and found that, under monolayer conditions, nucleation initially increased, but growth did not occur (Fig. 3**e**). In contrast, under multilayer conditions, nucleation initially increased during the early stage of stratification, followed by an increase in growth (Fig. 3**f**), consistent with observations in MDCK cell culture (Fig. 1**h**). These findings indicate that the presence of nuclear growth determines the occurrence of the monolayer-multilayer transition.

To understand the nucleation-growth characteristics of the simulated stratifications, we applied the JMAK model to fit the time evolution of ξ. The ξ values obtained from simulations were successfully fitted using Eq. 2 (Fig. 3**g**,**h**). In this fitting, we obtained ν values that varied from 1.0 to 2.69 (Fig. 3**i**). Notably, the region with low Γ and high λ had the closest Avrami exponent ($\nu \sim 2.29$) to that observed in the MDCK cell culture, involving a region with a similar number of layers (Fig. 2**i**). The decrease in ν accompanying an increase in Γ indicated that nucleation sites became more restricted as Γ increased. This restriction is consistent with the higher growth frequencies relative to nucleation frequencies seen in both simulations and experiments, supporting the analogical consistency of epithelial stratification with nucleation-growth physics.

Foam-geometric instability induces a nucleation-growth process

Epithelium stratifies via nucleation and growth while preserving heterogeneous structures (Figs. 1**e**, 2**j**). This indicates that individual cell delaminations occur in a dispersed manner due to local force balance, rather than simultaneously across the entire epithelium, as observed in spinodal decomposition. To investigate the mechanics behind cell delamination, we develop a theoretical model based on our previous theory[30]. In this model, we assumed a foam-like epithelial geometry using the 3D vertex model, focusing on the deformations of a single cell and its adjacent cells within a planar monolayer. By simplifying Eq. 3 with the mean-field approximation, we analytically derived the energy function for a delaminating cell (detailed in Materials and Methods).

We examined the dependence of stable cell shapes on apical line tension (λ), planar cell density (ρ), and the number of adjacent cells (n) by analyzing energy landscapes. Here, to describe the shape of a delaminating cell, we introduced the cell taper, d (Fig. 4**a**), which satisfies $-1 < d < 1$ when the cell is embedded in a monolayer and becomes -1 or 1 when it delaminates in the basal or apical direction. We calculated stable cell states by calculating d at points of energy minima, represented by d^*, and found that d^* shifted from $-1 < d^* < 1$ to $d^* = -1$ or $d^* = 1$, corresponding to transitions from embedded to delaminated states (Fig. 4**b–d**). Specifically, in relation to ρ and n, d^* bifurcated from $-1 < d^* < 1$ to $d^* = -1$ and $d^* = 1$ (Fig. 4**c–d**). These results indicate that mechanical instability is inherent in the foam-like epithelial geometry; either an increase in λ, an increase in ρ, or

a decrease in n leads to cell delamination. To validate this instability, we calculated the probability distribution of d in MDCK cell culture (Fig. 4**e**). We found a trimodal probability distribution around $d = -1$, 0, and 1, with two distinct gaps between $d = -1$ and 0 and between $d = 0$ and 1. This finding indicates that cells adopt either the embedded or delaminated state rather than staying in their intermediate state, implying that cells that lose the stability of the embedded state will immediately transition to the delaminated state. This is consistent with the hypothesis that an inherent instability leads cells to either an embedded or detached state.

While the dependences on λ, ρ, and n corresponded to the previous reports showing the contributors to cell delamination, including apical junctional forces[19–24], planar cell density[25–27], and cell geometry[28–30], the key driving force of epithelial stratification in MDCK cell culture (Fig. 1**b**) remained unclear. Therefore, we investigated each contributor. To determine whether λ drives epithelial stratification, we measured the apparent Young's moduli of the epithelium using AFM (Fig. 4**f**), which reflects cellular tensions[47]. We measured the modulus at apical junctions using a cantilever with a tip diameter of 60 nm, and tested the correlations between the modulus and the stratification ratio, ξ, finding that the apical junctional modulus certainly decreased with increasing ξ (Fig. 4**f**). These results suggest that apical junctional tension does not act as a key driving force behind stratification in MDCK cell culture.

To determine whether ρ drives epithelial stratification, we calculated the planar cell density, ρ, in MDCK cell culture, defined as the inverse of the average apical and basal surface area per cell, normalized by cell volume (detailed in Materials and Methods). We found a monotonic increase in ρ over time (Fig. 4**g**). Moreover, by correlating ξ with ρ over time, we assessed the dependence of ξ on ρ (Fig. 4**h**) and found that ξ increased with ρ in a switch-like manner, well-fitted by a sigmoidal curve. This finding aligns with previous studies highlighting the influence of cell density on individual cell delamination[25–27] as well as our analytical calculations (Fig. 4**b**). These results suggest that planar cell density, rather than apical junctional tension, is the key driving force behind epithelial stratification in MDCK cell culture. Note that these measurements were conducted in MDCK cell culture, so that both apical junctional tension and cell density may be key driving forces in other epithelial stratifications.

Additionally, to investigate the influence of n on stratification, we observed the changes in cell geometries during the delamination process in both simulations and experiments (Fig. 4**i–n**). During stratification, each cell gradually reduced the number of adjacent cells and lost either its apical or basal side to delaminate from the monolayer (Fig. 4**i**,**j**), which aligns with our theory (Fig. 4**e**). Interestingly, during this delamination process, we found that cells formed a scutoid geometry[48], which occurred when the cell-cell contacts differed between the apical and basal sides; for example, blue and yellow

cells made contact on the apical side, whereas red and green cells made contact on the basal side (Fig. 4**k–l**). In these situations, the connectivity between cells switched at the lateral boundary surfaces between cells (Fig. 4**m–n**). Scutoid formation was necessary to change the 3D foam-like arrangement of cells in a planar cell monolayer, which enabled cells to reduce the number of adjacent cells. This reduction triggered mechanical instability (Fig. 4**d**), thus promoting delamination.

These results show that mechanical instability inherent in the foam-like epithelial geometry induces a nucleation-growth process. This instability can be evoked by increases in apical junctional tension or planar cell density, whereas the MDCK cell stratification observed in our study was driven by an increase in cell density. During cell delamination, cells gradually lose either their apical or basal side while forming a scutoid geometry to reduce the number of adjacent cells, which also contributes to the evocation of instability. The accumulation of cell delaminations leads to the phase transition of the epithelial structure from monolayer to multilayer.

Nucleation-growth concept applies to embryogenesis and carcinogenesis

To determine whether the nucleation-growth concept applies to embryogenesis and carcinogenesis, we examined the epithelial stratification processes during mouse skin development and malignant transformation of cancer in mouse intestinal organoids (Fig. 5). Skin development involves epithelial stratification, where the epidermal monolayer transitions to a multilayer structure as basal layer cells delaminate and differentiate into periderm cells[12,49,50] (Fig. 5**a**). This stratification initiates at the limb and tail tips and gradually extends across the body[49]. However, the mechanism underlying the spread of the stratification domain remains poorly understood. To address this issue, we analyzed the dorsal skin of mouse embryos (Fig. 5**a**, see Materials and Methods), identifying three distinct structural states from embryonic day (E)9.5 to E13.5: near monolayer, mixed layer, and multilayer (Fig. 5**b**). Spatial analyses of delaminated cells in the epidermis revealed two patterns: dispersed and clustered arrangements (Fig. 5**c**). These observations indicate that epidermal stratification proceeds through both nucleation and growth, rather than through continuous growth of multilayered domains. Moreover, stratification ratios increased from approximately 0.08 to 1.0 during the monolayer-to-multilayer transition (Fig. 5**d**), while the epidermis maintained amorphous-like structural characteristics (Fig. 5**e**). These findings suggest that the concept of a phase transition, involving nucleation and growth, is applicable to skin development.

To investigate whether this concept also applies to cancer progression, we studied early-stage cancer cell invasion, where precancerous epithelial cells undergo abnormal stratification leading to invasion. For this purpose, we used key cancer-driving mutations in mouse intestinal cancer organoids:

Apc (A), Kras (K), Tgfrbr2 (T), Trp53 (P), and Fbxw7 (F)[51] (see Materials and Methods). A previous study showed that exposure to activin A in culture (Fig. 5**f**) induces malignant transformation in these organoids, mimicking *in vivo* cancerous behaviors[52]. Specifically, organoids cultured without activin A formed spherical cysts, whereas those exposed to activin A displayed malignant morphologies, such as heterogenous spherical or protruded, star-like structures (Fig. 5**g**). At 0 hours, organoids exhibited a monolayer structure with a few dispersed delaminated cells. By 48 hours post-transformation, these organoids transitioned to a multilayered structure with clustered delaminated cells (Fig. 5**h**). Consistently, stratification ratios increased from approximately 0.02 to 0.2 during this transition (Fig. 5**i**). Moreover, the amorphous-like structural characteristics were maintained both before and after transformation (Fig. 5**j**). These results suggest an analogical parallel between the phase transition involving nucleation and growth and intestine cancer transformation and demonstrate that the nucleation-growth concept applies not only to MDCK cell culture but also to embryogenesis and carcinogenesis.

Discussion

In this study, we elucidated the physical mechanism underlying epithelial stratification, specifically the transition from a monolayer to a multilayer structure (Fig. 6). This is like a first-order phase transition that maintains amorphous structures. It is accompanied by nucleation and growth and is governed by the growth rate of delaminated domains rather than nucleation. The elementary process of both nucleation and growth, namely single-cell delamination, is induced by the mechanical instability inherent in foam-like epithelial geometry. This instability can be evoked by either apical junctional tension or planar cell density, under regulation of various cell behaviors such as actomyosin contractility[19–24], cadherin adhesion[53–55], and cell proliferation[25–27]. The instability can also be triggered by a decrease in the number of cells adjacent to a delaminating cell, which is mediated by the formation of cell scutoid geometry. Overall, we demonstrated that epithelial stratification can be conceptualized as a phase transition governed by nucleation and growth. This analogy could apply to general epithelial stratification, including embryogenesis and carcinogenesis.

The nucleation-growth process is a well-established concept in solid matter physics. Yet, to the best of our knowledge, this is the first report of its application in the context of epithelial stratification. Traditionally, crystallization of materials such as water and metals is governed by nucleation and growth, typically induced by an increase in material density[56]. Our research demonstrated that epithelial stratification shares these characteristics (Figs. 1–3), highlighting their common analogy with nucleation-growth process in a wide range of biological phenomena, including embryogenesis and carcinogenesis (Fig. 5). Based on this analogy, we can apply methods used in the physical understanding of nucleation and growth to investigate epithelial stratification. For instance, using the JMAK model[38], we evaluated whether nucleation or growth governs each stratification process. Specifically, frequent growth was observed in MDCK cell culture (Fig. 1**c**,**d**), whereas nucleation could be dominant in other phenomena. This analysis will be helpful in exploring cell behaviors in the developmental mechanisms of various epithelia[1–9], teratogenic diseases caused by stratification failure, such as lissencephaly and neuronal migration disorders[57], and malignant transformation of cancer diseases initiated by stratification[13]. Therefore, there is potential applicability of existing methods for nucleation and growth to deepen the understanding of a wide range of phenomena induced by epithelial stratification, including embryogenesis and carcinogenesis.

Epithelium maintains amorphous-like structures during stratification (Figs. 1**e**, 2**j**, 4**e**, **j**). Similar phase transitions have been observed in various materials, such as ice[58], silicon[59,60], and silica[61,62]. However, the mechanism inducing epithelial stratification differs from the supercooling-induced transitions in conventional materials. Instead, epithelial stratification is induced by a local force

balance among cells, involving a mechanical instability. This instability arises from the inherent flexibility of foam geometry, specifically cell deformation (Fig. 4). This structural flexibility enables cells to modify epithelial properties through behaviors such as apical junctional tension, planar cell density, and cell geometry, which evoke instability and lead to stratification. Consequently, the foam-like geometry imparts unique properties to epithelia, providing a fundamental framework for investigating the mechanisms underlying epithelial stratification.

While this study provides a conceptual understanding of epithelial stratification, it is important to acknowledge its limitations. Most experiments were limited to a simple MDCK cell culture system, which allows clarification of the conceptual findings but raises questions about their applicability to the complexities of embryonic and cancerous tissues. Additionally, our model simplifies the problem of energy minimization for a fixed number of cell populations with uniform properties. This simplification allows clarification of the fundamental understanding, whereas the roles of more complex cell behaviors remain unclear, such as cell proliferation, cell motility, and the diversity in cell properties caused by differentiation, all of which could play significant roles in regulating stratification in broader biological scenarios[14–16,63–65]. Therefore, the relationship between our experiments and simulations remains primarily qualitative. This study marks the beginning of a multiscale physical exploration of the entire stratification process. Incorporation of these additional cellular behaviors in future research could lead to a more quantitative understanding of critical biological processes such as embryonic development and cancer progression.

Acknowledgments

We thank all the members of the Okuda Laboratory for discussions, A. Matsuoka for help with image analysis, and M. Nakayama, D. Wang, and H. Oshima at Kanazawa University for discussions. This work was supported by the WISE Program for Nano-Precision Medicine, Science, and Technology of Kanazawa University, Ministry of Education, Culture, Sports, Science and Technology (MEXT; to A.T.); the Japan Science and Technology Agency (JST), CREST [Grant No. JPMJCR1921, JPMJCR24B2]; the Japan Society for the Promotion of Science (JSPS), KAKENHI [Grant No. 21H01209, 21KK0134, 22H05170, 24H01398, 24H01937 (to S.O.), 24KJ0090 (to S.H.)]; the Program for Technological Innovation of Regenerative Medicine Grant 23bm0704065h0003 (to S.O.), 21bm0704060h0001, and 24bm1123049h0001 (to I.I.) from the Japanese Agency for Medical Research and Development (AMED), and the World Premier International Research Center Initiative, MEXT, Japan (to S.O.).

Contributions

S.F.: data curation, formal analysis, investigation, methodology, software, validation, visualization, and writing (original draft and revised draft). R.D.: data curation, formal analysis, visualization. D. W., T.I., P.L.: data curation, formal analysis, investigation, validation, and visualization. R.Y., K.O.: investigation, validation, supervision. S.H.: formal analysis, investigation, methodology, software, validation. K.K.: resources and validation. A.S., I.I.: investigation. T.F., H.F.: funding acquisition, project administration, supervision. S.O.: conceptualization, data curation, funding acquisition, methodology, project administration, software, supervision, visualization, and writing (original draft and revised draft).

Competing interests

All authors declare no competing interests.

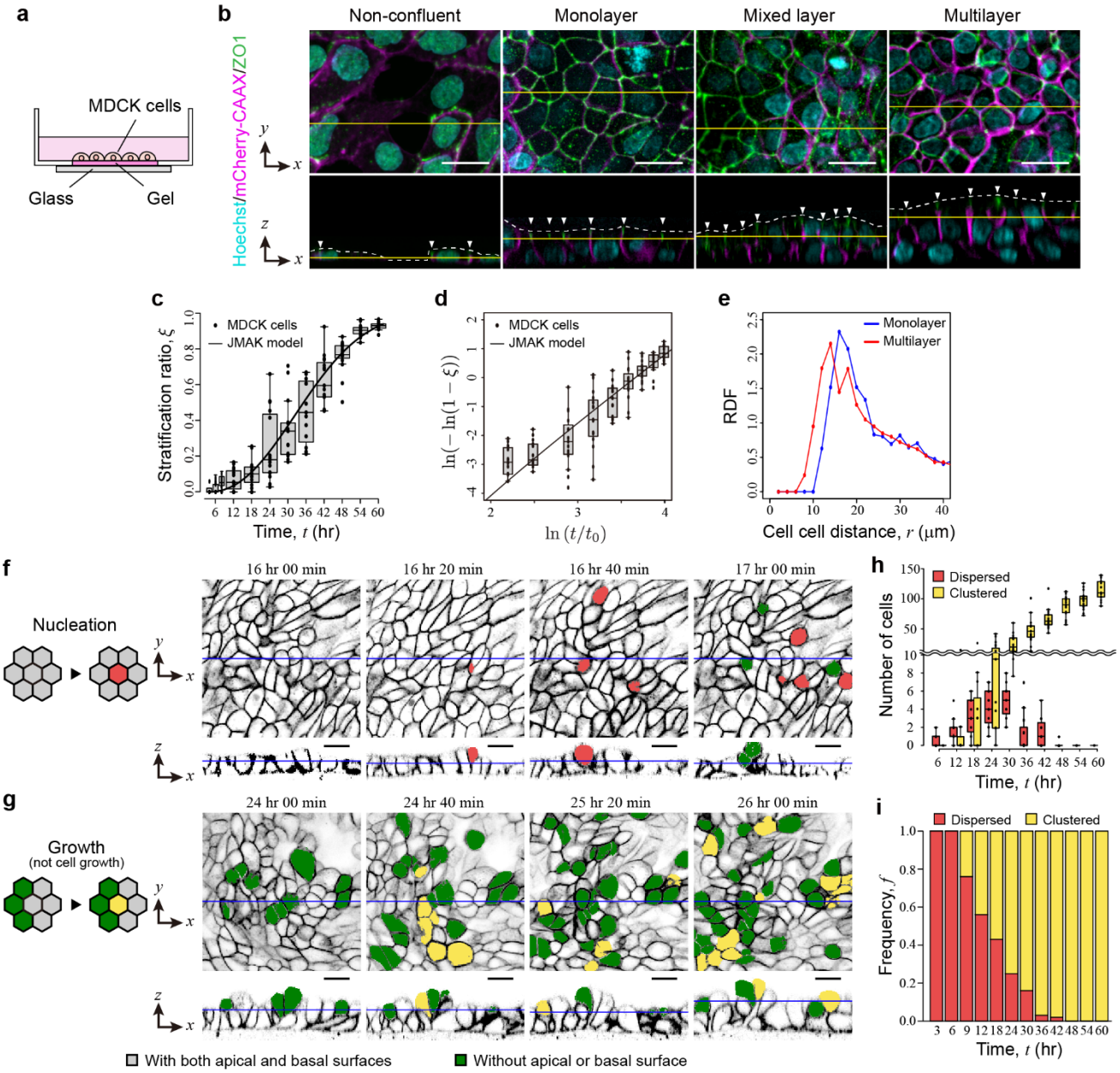

Fig. 1: Epithelial cells stratify through a nucleation-growth process. (a) Schematic illustration of the MDCK cell culture setup used to observe epithelial stratification. (b) Fluorescence images of MDCK cells stably expressing mCherry-CAAX, stained with a ZO1 antibody and Hoechst. The top panel shows the *z*-projection, and the bottom panel displays a single *xz*-view image along the yellow line in the top panel. The white arrow highlights the ZO1 signal in the *xz*-view, and the dotted line marks the apical surface. Scale bar: 20 μm. (c and d) Linear and Avrami plots of the stratification ratio, ξ ($N \geq 5$). In (c) and (d), solid lines represent fitted curves based on the JMAK model (refer to Materials and Methods). (e) Radial distribution function (RDF) of cells in monolayer and multilayer structures ($N \geq 17$). (f and g) Schematic illustration (left) and corresponding experimental images (right) depicting nucleation and growth during stratification. Red cells represent newly delaminated

cells appearing in the monolayer, and yellow cells represent newly delaminated cells adjacent to existing ones. Scale bar: 20 µm. (h) Temporal changes in the number of dispersed versus clustered delaminated cells. (i) Temporal changes in the ratio of dispersed and clustered delaminated cells. Plots in (c, d, e, h, and i) include data from 15 images. Box plots in (c, d, and h): center: median; bounds, 25th and 75th percentiles; whiskers, min and max.

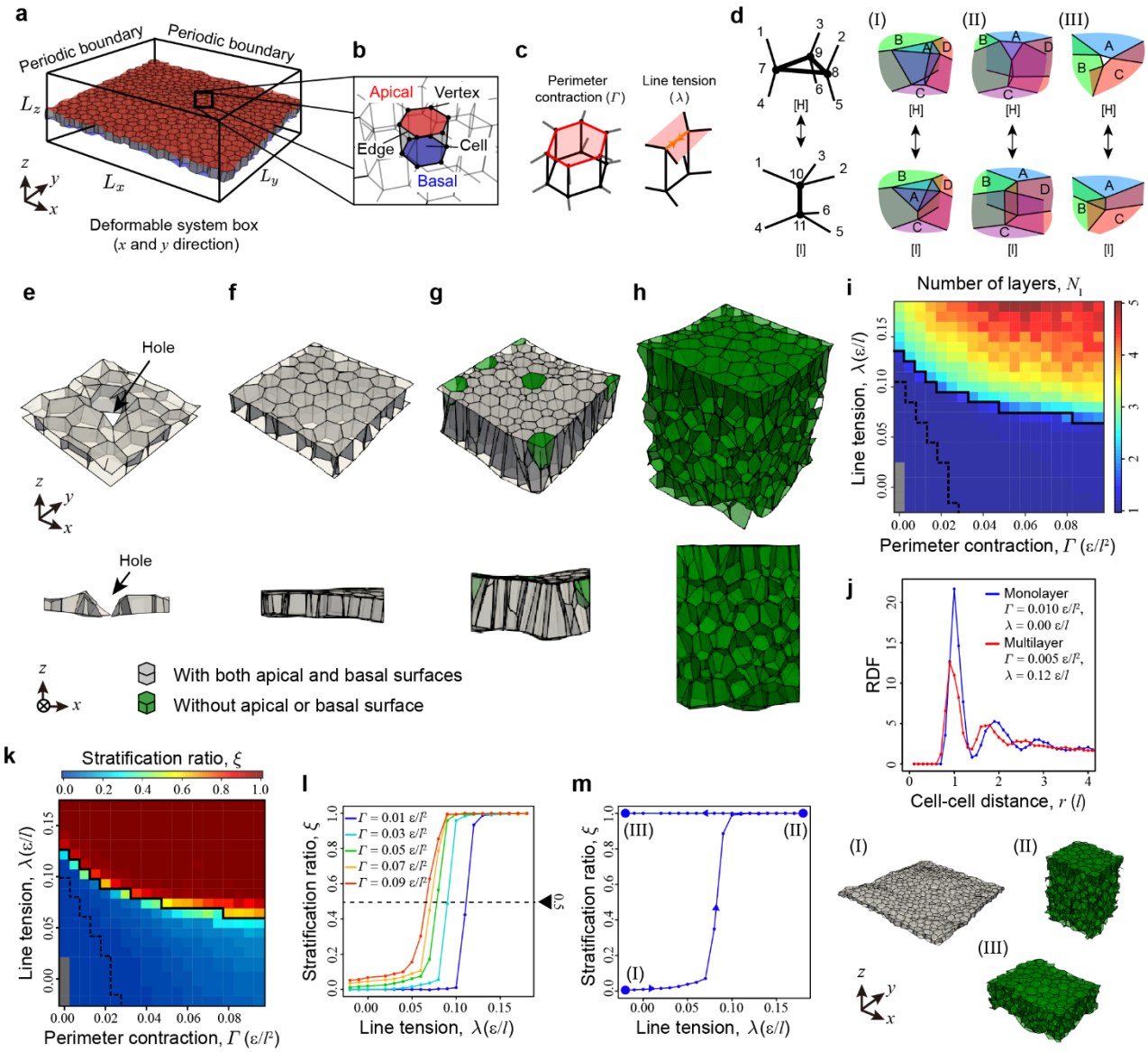

Fig. 2: Three-dimensional vertex model reveals a phase transition from monolayer to multilayer phase. (a) Initial monolayer epithelial sheet condition in 3D space, where the system box is deformed by axial stress in the *xy* plane. (b) Enlarged image of a single cell within the epithelial sheet; surface colors indicate the apical (red), lateral (gray), and basal (blue) surfaces. (c) Schematic illustrations of apical junctional forces acting on individual apical cell perimeters: apical perimeter contraction, Γ (left), and individual apical cell edges: apical edge tension, λ (right). (d) Definition of topological operations between patterns [H] and [I], including examples of cell extrusion from a monolayer (I), cell rearrangement within the sheet plane (II), and sheet collapse through hole formation (III). (e–h) Epithelial structures after relaxation, showing different states: collapse (e), monolayer (f), partial multilayer (g), and multilayer (h), induced by varying apical junctional forces. The parameters used

were set to $\Gamma = 0, \lambda = 0$ (e), $\Gamma = 0.015\ \varepsilon/l^2, \lambda = 0$ (f), $\Gamma = 0.075\ \varepsilon/l^2, \lambda = 0.03\ \varepsilon/l$ (g), and $\Gamma = 0.065\ \varepsilon/l^2, \lambda = 0.13\ \varepsilon/l$ (h). (i) Number of layers, N_l, with respect to Γ and λ. (j) Radial distribution function (RDF) of cells. (k) Stratification ratio, ξ, with respect to Γ and λ. In (i and k), solid and dotted lines indicate boundaries among the multilayer ($\xi > 0.5$), monolayer ($0.5 \geq \xi \geq 0.1$), and complete monolayer ($0.1 > \xi$) phases. Gray indicates collapse phase. (l and m) Stratification ratio, ξ, as a function of λ. In (m), epithelial structures at the indicated points I–III are shown on the right. The results between points I and III were calculated starting from the monolayer initial condition shown in (a), and those between points II and III were obtained using the multilayer initial condition at point II. Colors in (i) and (k) indicate the average values of the five initial conditions. Each data point in (i–m) indicates the average values calculated from the five initial conditions. In (m), data between points (I) and (II) are calculated from the initial monolayer condition, while those between points (II) and (III) are from the initial multilayer condition obtained at point (II).

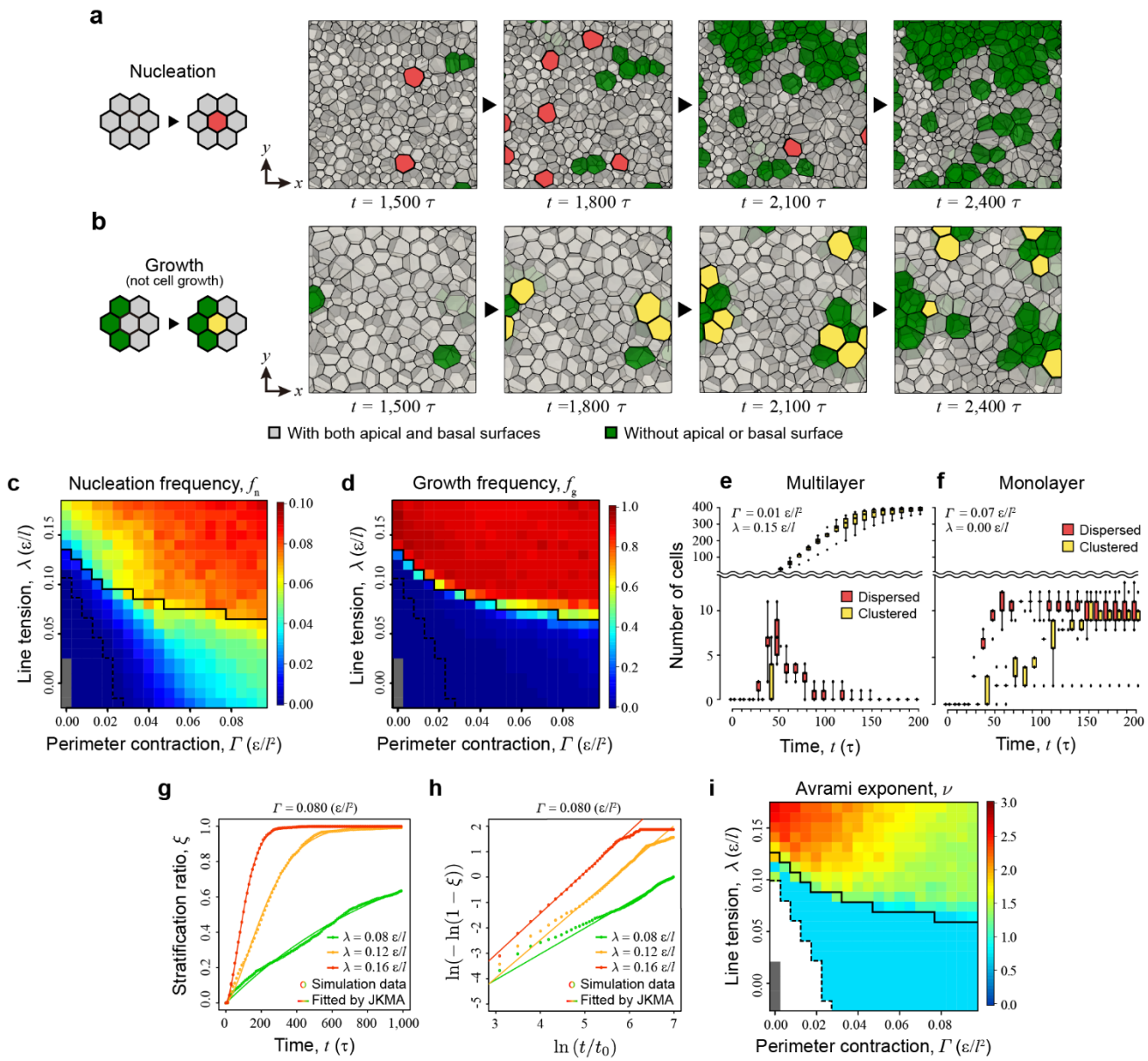

Fig. 3: Three-dimensional vertex model recapitulates nucleation-growth process, revealing growth governing stratification. (a and b) Schematic illustration (left) and corresponding simulation results (right) depicting nucleation and growth during stratification. Red cells represent newly delaminated cells appearing in the monolayer, and yellow cells represent newly delaminated cells adjacent to existing ones. (c and d) Nucleation ratio, f_n, and growth ratio, f_g, (e and f) with respect to apical perimeter contraction, Γ, and apical edge tension, λ. (e and f) Temporal changes in the number of dispersed versus clustered delaminated cells under multilayer and monolayer conditions, respectively. (g and h) Linear and Avrami plots of the stratification ratio, ξ, as a function of time, t, respectively. Dotted lines indicate simulation data. Solid lines indicate lines fitted by the JMAK model. (h) Avrami plot of stratification data obtained from a numerical simulation. The solid line indicates the line fitted by the JMAK model. (i) Avrami exponent, ν, with respect to Γ and λ. The solid line

indicates the boundary between the monolayer and multilayer structure. In (c), (e), and (i), solid and dotted lines indicate the boundaries among multilayer ($\xi > 0.5$), monolayer ($0.5 \geq \xi \geq 0.1$), and complete monolayer ($0.1 > \xi$) phases. The gray color indicates the collapse phase. The colors in (c), (e), and (i) indicate the average values of the five initial conditions. The colors and dots in (c–i) indicate the average values of the five initial conditions. Box plots in (e and f): center: median; bounds, 25th and 75th percentiles; whiskers, min and max.

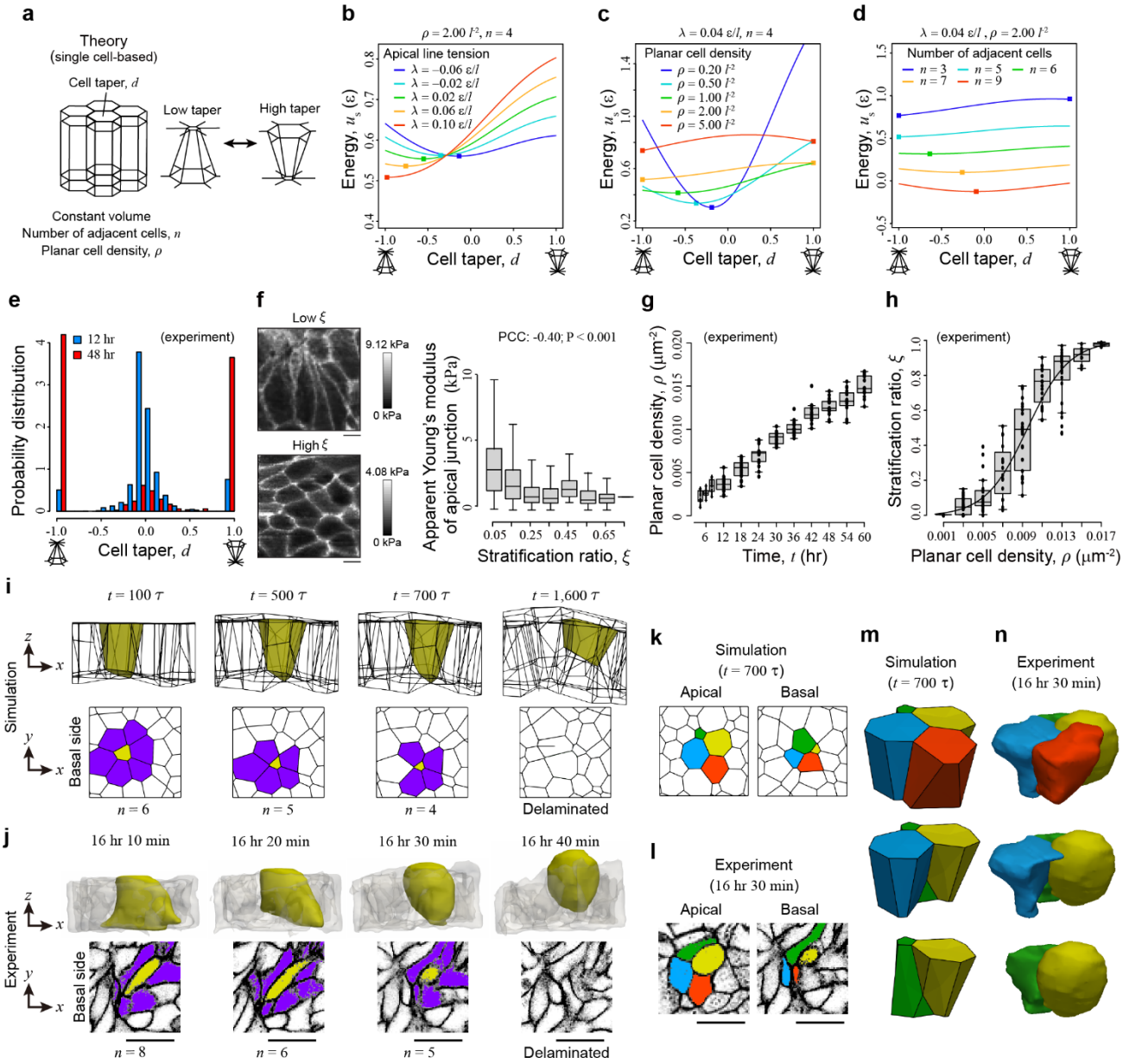

Fig. 4: Foam-geometric instability induces epithelial stratification with scutoid formation. (a) Theoretical model describing the epithelial sheet 3D foam geometry. A single center cell is embedded within a sheet, modeled as a regular frustum, with its geometry uniquely determined by the number of adjacent cells, n, planar cell density, ρ, and cell taper, d. (b–d) Energy landscapes as a function of d, with respect to apical line tension λ, ρ, and n, respectively, derived from the theoretical model. Squares indicate energy minima. (e) Probability distribution of cell taper calculated from experimental MDCK data at 12 and 48 hours of culture ($N \geq 5$). (f) Apparent Young's modulus maps with high and low ξ (left). Apparent Young's modulus of apical junction as a function of ξ, obtained from AFM measurements ($N = 19$) (right). Scale bar: 10 μm. (g and h) Stratification ratio, ξ, as a function of time, t, and ρ, respectively ($N \geq 15$). The solid line in (h) represents a fitted sigmoid function. (i and j) Delamination processes in the 3D vertex model (i) and MDCK cell culture (j). The top images depict

3D views, and the bottom images show apical cell geometry, with the number of cells adjacent to delaminating cells, n, indicated below. Yellow highlights cell delamination toward the apical side as cells lose basal surfaces, and purple marks cells adjacent to delaminating ones. Scale bar: 10 μm. (k–n) Scutoid formation during cell delamination in the 3D vertex model (k, m) and MDCK cell culture (l, n). Identical cells are indicated by the same colors, with the green cell forming a scutoid geometry. (k and l) Cell geometries on the apical and basal sides. Scale bar: 10 μm. (m and n) 3D geometries of cells colored as in (k and l). The plots in (f, g, and h) include data from more than 15 images. Box plots in (f–h): center, median; bounds, 25th and 75th percentiles; whiskers, min and max. In (f), individual data points are not shown due to the presence of 10,000 points. In (f), Pearson correlation coefficients between the apparent Young's modulus and ξ were calculated; P-values were obtained using Student's t-test for non-correlation.

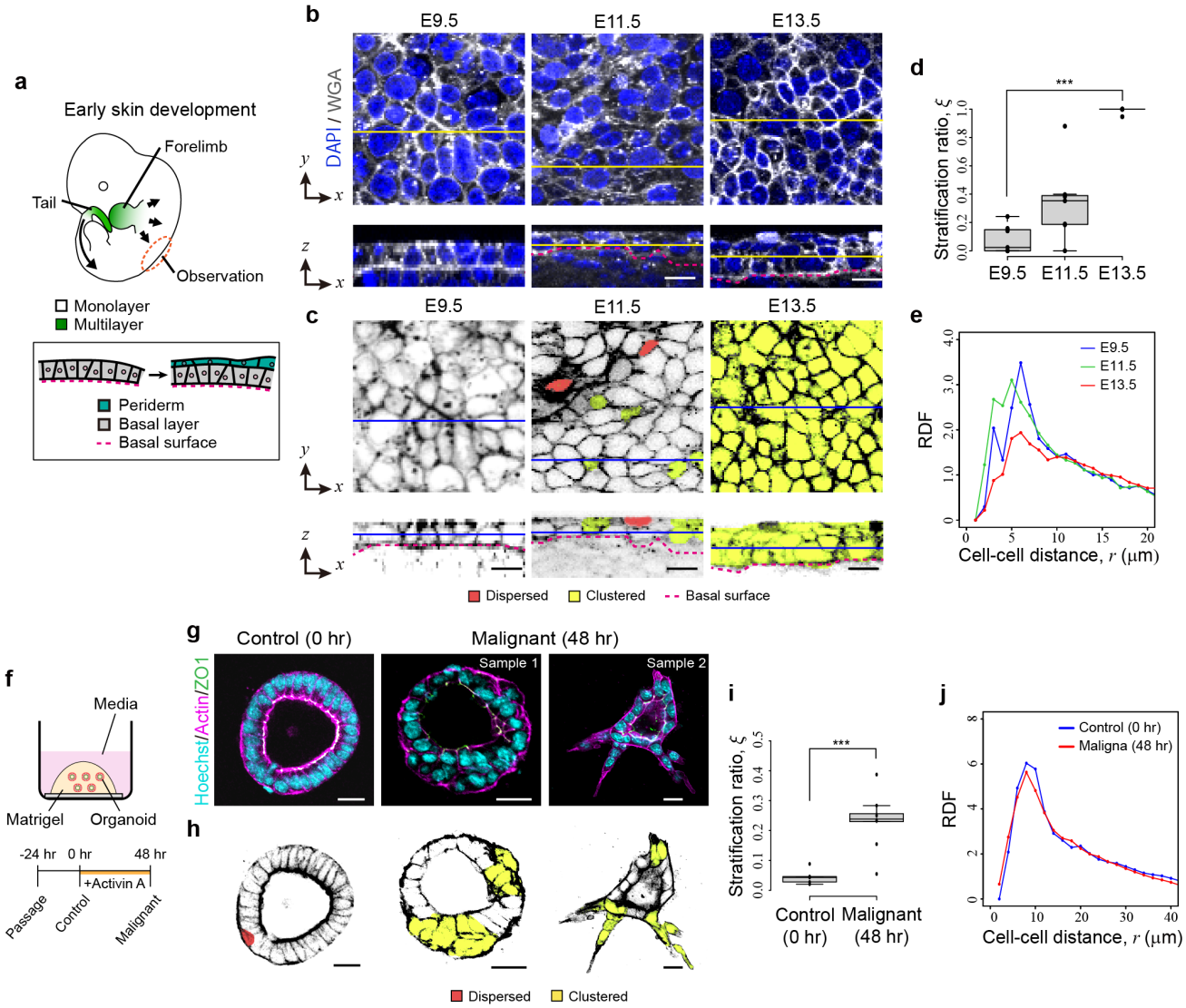

Fig. 5: Nucleation-growth concept applies to embryogenesis and carcinogenesis. (a–e) Data for mouse skin development. (a) Schematic illustration of epidermal stratification progression in the entire mouse embryo. (b and c) Fluorescent section images of mouse skin and modified images highlighting delaminated cells. The skin is a monolayer in E9.5, mixed layer in E11.5, and multilayer structure in E13.5. The top panel shows the *z*-projection, and the bottom panel displays a single *xz*-view image along the line in the top panel. The dotted lines mark the basal surfaces. Scale bar: 10 μm. In (b), epidermises were stained with wheat germ agglutinin (WGA) antibody and DAPI. (d) Stratification ratio, ξ, in each stage. (e) Radial distribution function (RDF) in each stage. (f–j) Malignant transformation of intestinal cancer organoid data. (f) Schematic illustration of cancer organoid culture and malignant phenotype induction. (g and h) Fluorescent section images and modified images highlighting delaminated cells, respectively. In (g), organoids were stained with a ZO1 antibody, phalloidin, and Hoechst. Scale bar indicates 20 μm. (i) Stratification ratio, ξ, under control and malignant induction. (j) RDF of control and malignant induction. In (c and h), dispersed and clustered

delaminated cells are colored red and yellow, respectively. Plots in (d, e, i, and j) include data from more than five images. Box plots in (e, j): center: median; bounds, 25th and 75th percentiles; whiskers, min and max; ***$P < 0.001$ (Welch's t-test).

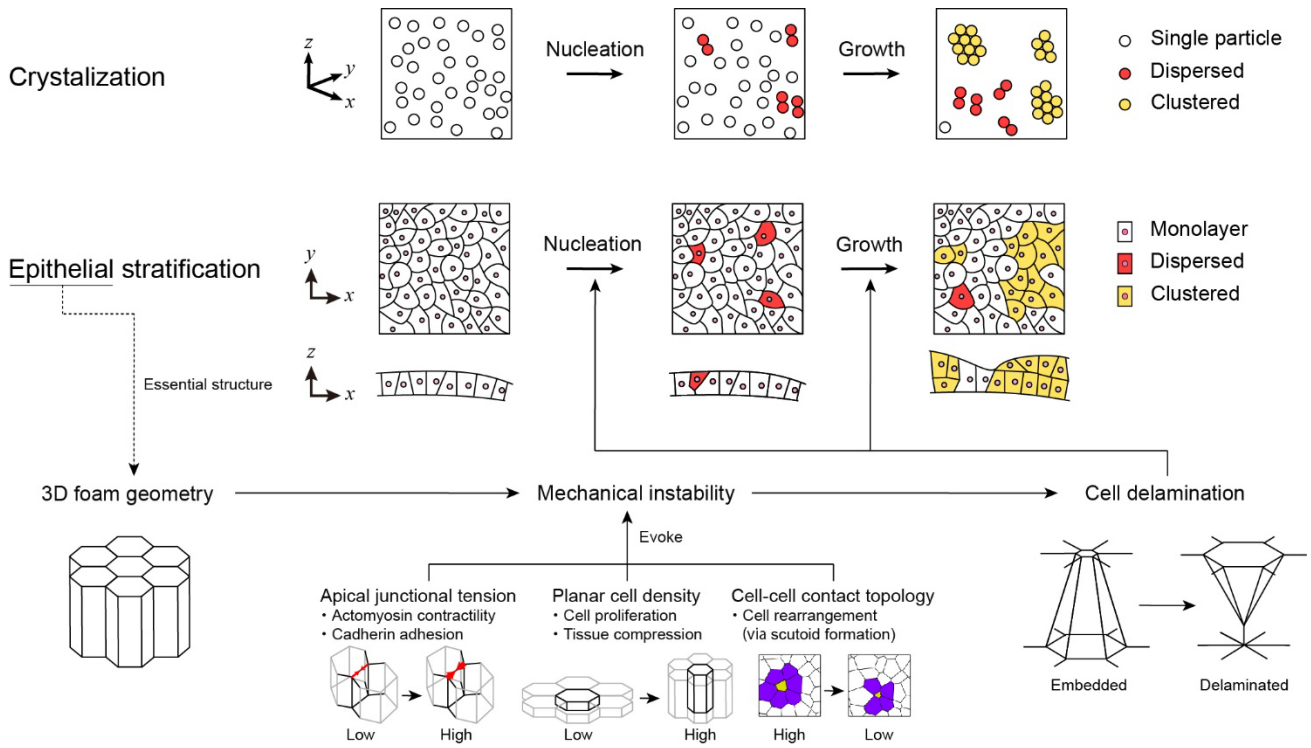

Fig. 6: Epithelial stratification proceeds via nucleation and growth induced by foam-geometric instability. Epithelial stratification can be understood as a phase transition, such as crystallization, that involves a nucleation-growth process. In this framework, stratification represents a structural transition from a monolayer to a multilayer configuration. The fundamental process driving this transition is cell delamination, which arises from mechanical instability inherent in the 3D geometry of the epithelial sheet. This instability can be evoked by various factors, including increased apical junctional tension due to actomyosin contractility and cadherin-mediated adhesion, increased planar cell density resulting from cell proliferation and tissue compression, and changes in cell-cell contact topology caused by rearrangements associated with scutoid formation.

Materials and Methods

MDCK cell line

Madin-Darby canine kidney (MDCK, type I) cells stably expressing mCherry-CAAX were provided by Dr. Kajiwara (Osaka University, Osaka). The cells were cultured in Dulbecco's Modified Eagle's medium (DMEM, Nacalai Tesque) supplemented with 10% fetal bovine serum (FBS, Gibco) and 1% penicillin-streptomycin (Wako). Cultures were maintained in a 5% CO_2 incubator at 37°C.

MDCK cell culture to observe epithelial stratification

A 35-mm glass-bottom imaging dish (Matsunami) was coated with 30 μL of Cellmatrix Type I-A (Nitta Gelatin). A cell suspension containing 1.8×10^5 cells in 250 μL of DMEM (Nacalai Tesque) supplemented with 10% FBS (Gibco) was added to the dish and incubated. After 4 hours, 2 mL of the medium was added. The dish was incubated until 60 hours after addition of the cell suspension.

Immunostaining of MDCK epithelium

Cells were fixed in 4% paraformaldehyde (PFA) (Fujifilm Wako) in phosphate-buffered saline (PBS) for 30 minutes at room temperature (RT), followed by two washes with PBS. The cells were permeabilized with 0.5% Triton-X in PBS for 2 minutes. After three washes with PBS, the samples were blocked with 4% bovine serum albumin (BSA)/PBS for 10 minutes and incubated for 1.5 hours with anti-rabbit ZO-1 (1:100 dilution). After washing with PBS, the samples were incubated for 1.5 hours with Goat anti-Rabbit IgG 488 H&L antibody (1:100 dilution, ab150077, Abcam), Phalloidin-iFluor 647 Conjugate (1:1000 dilution, 20555, Cayman), and Hoechst (1:1000 dilution, 343-07961, Fujifilm Wako). Following three washes with PBS, the samples were mounted in 50% glycerol in PBS. Fluorescent images were acquired using a BZ-X810 microscope (Keyence).

Observation and quantification of MDCK epithelium

Z-stack imaging was performed at each time point using a BZ-X810 microscope (Keyence) equipped with a 60× (NA 0.45) objective. Images were captured using the 2× zoom function with a step size of 0.4–2 μm. Five images were obtained from the center to the periphery of the dish at each time point.

The stratification ratio, ξ, was calculated using Eq. 1. For this calculation, cells were categorized into four types: cells with both apical and basal surfaces, cells with either apical or basal surfaces, and cells with neither apical nor basal surfaces. The presence of apical and basal surfaces was manually identified using an Advanced Observation Module (BZH4XD, Keyence), based on the mCherry-

CAAX intensity. ξ was calculated at every time point and fitted with the JMAK model in Eq. 2 using a nonlinear least squares method to obtain the parameters K, n, and t_0. Moreover, delaminated cells were classified as nucleated and clustered based on the presence of adjacent delaminated cells using Fiji software. Cluster size was calculated as the number of delaminated cells comprising each isolated cell cluster.

Planar cell density, ρ, was determined by counting cells based on the mCherry-CAAX intensity. The number of cells was calculated as $N_\mathrm{c} + N_\mathrm{e}/2$, where N_c is the number of single cells fully located within an image and N_e is the number of cells partially crossing the image edge. ρ was calculated by dividing the number of cells by the total area of the image. Moreover, the correlation between ξ and ρ was determined by calculating ξ and ρ for individual images.

Observation and visualization of single MDCK cell shapes

Time-lapse imaging was performed using an FV 3000 confocal microscope (Olympus) equipped with a GaAsP detector (FV31-HSD, Evident) and a dichroic mirror (U-FBNA, Olympus) in a humidified 5% CO_2 atmosphere at 37°C. Images were captured with a step size of 0.43 for 6 hours, at 10-minute intervals. Using the mCherry-CAAX intensity, individual cells were manually masked using Fiji and Drishti v. 3.2. The masked images were visualized using ParaView (Kitware Inc.) and Imaris viewer (Bitplane).

Immunostaining and observation of mouse embryonic skin

To prepare mouse embryonic skin tissue samples, pregnant Jcl:ICR mice (CLEA Japan, Inc.) were euthanized by cervical dislocation, and embryos at E9.5, 11.5, and 13.5 were collected. The head, tail, limbs, and internal organs were removed, leaving the skin tissue, which was fixed with 4% PFA in PBS for 1 hour at 4°C. Following fixation, the tissues were washed with PBS and blocked with 1% BSA/PBS for 1 hour at 4°C. Nuclei were stained with DAPI (1:1000; Dojindo; D523), and plasma membranes were labeled with wheat germ agglutinin (WGA, 1:200; Invitrogen; W32466) for 2 hours at RT. The tissues were then washed with PBS and immersed in 60% 2,2'-thiodiethanol (FUJIFILM; 201-04193) in PBS for 1 hour at RT to enhance optical clarity. Fluorescence signals were captured with a TCS SP8X confocal microscope (Leica) with a 40× oil immersion objective lens (Leica, HC PL APO 40×/1.30 Oil CS2) and LAS X software (version [BETA] 3.5.7.23723).

Quantification of mouse embryonic skin

The stratification ratio, ξ, was calculated using Eq. 1. For this calculation, we counted the total number

of cells constituting epidermis in 3D stacked images based on both DAPI and WGA signals using LAS X. Delaminated cells in skin tissue were defined as cells without apical or basal surfaces, and the number of cells was manually counted. Basal surfaces were defined as having high area fluorescence intensity of the WGA signal. Seven samples were randomly selected for each stage.

Intestinal cancer cell line

Intestinal cancer cells, provided by Dr. Oshima (Kanazawa University, Kanazawa), were derived from mouse somatic cells that had been transduced with cancer mutations, as previously described[51]. These cells were originally harvested from small intestinal tumors in mouse models that carried a combination of key colorectal cancer driver mutations — Apc (A), Kras (K), Tgfrbr2 (T), Trp53 (P), and Fbxw7 (F) — in their intestinal epithelial cells. These cells reflect *in vivo* malignant behaviors, serving as a realistic model to study cancer progression and transformation.

Intestinal cancer organoid culture

Intestinal cancer organoids were prepared using a previously described method[66]. Intestinal cancer cells were enzymatically or mechanically dissociated into either single cells or small aggregates and then cultured at 37°C in a 48-well dish (Corning) embedded in 30 µL of Matrigel (Corning) surrounded by 300 µL of a media cocktail for organoid culture. The media contained Advanced DMEM/F-12 medium (Gibco), supplemented with 1% 100X GlutaMAX™ (Gibco), 1% 100X N-2 (Gibco), 1% 1M HEPES buffer solution (Gibco), 1% penicillin/streptomycin solution (Wako, 100X), 2% 50× B-27 supplement (Gibco), and 0.1% 1 mM N-acetylcysteine (Sigma). Organoids were passaged every 2–3 days for maintenance by resuspending them while embedded in fresh Matrigel with media in a new well of a culture dish.

Malignant phenotype induction of intestinal cancer organoids

Malignant phenotypes were induced using a previously described method[52]. Intestinal organoids were passaged into a Collagen I matrix (Wako) using the media cocktail for organoid culture. After 24 hours of incubation at 37°C, the medium was replaced with fresh medium with an additional 20 ng/mL of the induction factor activin A (Cosmobio).

Intestinal cancer organoid immunostaining and observation

Organoids were fixed by emersion in 4% PFA (Wako) at RT for 30 minutes. Samples were then washed three times in PBS before permeabilization and blocking. Permeabilization was a two-step

process starting with emersion in 0.5% TritonX-100 (Fisher)/PBS for 30 minutes at 4°C. Next, samples were permeabilized in PBS containing 0.1% BSA (Wako), 0.2% TritonX-100, and 0.05% Tween20 (Wako) at RT for a minimum of 2 hours. The samples were blocked by incubation in 1% BSA solution for 1 hour at RT. They were then immunostained overnight at 4°C with nucleus (Cellstain Hoechst 33258, Wako, 1:300 dilution), F-actin (Phalloidin iFluor 647 Conjugate, Cayman, 1:500 dilution), and ZO1 (ZO-1 Polyclonal Antibody, Invitrogen, 1:100) antibodies diluted in 1% BSA. Secondary antibody (Goat anti-Rabbit IgG H&L Alexa Fluor®488, Abcam, 1:200 dilution) incubation was performed under the same conditions as for primary antibodies after permeabilization in 0.1% BSA (Wako), 0.2% TritonX-100, and 0.05% Tween20 (Wako) buffer at RT for a minimum of 2 hours. Following immunofluorescence assays, fluorescent imaging of samples was performed using a confocal microscope (FV3000, Olympus) equipped with a 20× objective lens (20x-UPlanXApo, Olympus). Three-dimensional projections of images were reconstructed using ImageJ for analysis.

Intestinal cancer organoid stratification ratio calculation

The stratification ratio, ξ, was calculated using EQ. 1. The total number of cells constituting each organoid in 3D stacked images was counted based on both F-actin and Hoechst signals using Fiji software. Delaminated cells in organoids were defined as cells without ZO-1 signal, and the number of cells was manually counted. For the control group, five organoids were randomly selected from three separate culture dishes. For the activin-treated group, nine organoids were randomly selected from five dishes.

RDF analysis

The RDF expresses the statistical distribution of the positions of other particles around one particle. By taking the position of a particle as the origin and letting $N_{\mathrm{g}}(r)$ be the mean number of particles in the spherical shell of the radius $(r, r + \mathrm{d}r)$, the RDF is defined by

$$g(r) = \frac{N_{\mathrm{g}}(r)}{4\pi\rho_{\mathrm{N}} r^2 \Delta r}, \tag{4}$$

where ρ_{N} is the mean number density of the system.

In the numerical simulations, cells were considered particles, and the position of each centroid was calculated. The distance between cells was calculated using the centroid position. The mean number density was calculated from the average of the number density of each cell. The number density was calculated by dividing the number of cells by the volume in a sphere whose radius was half the length of the shorter side of the boundary size, L_x or L_y. This radius assumption ensures that

the same cell is not counted twice by periodic boundaries. Then, we calculated this for all 401 cells and determined the average.

In the MDCK cell, mouse skin tissue, and intestinal organoid experiments, cell location was derived from the position of the nucleus. Nuclei centroid positions were detected in 3D images using the Hessian-based algorithm as described[67]. For nuclei-stained images, the difference of Gaussian filter was applied to enhance the variation in the nuclei size scale. Points with a positive definite Hessian matrix in the image were considered nuclei candidates. Connected components with small size or low median intensity were considered to be noisy candidates and were removed. The centroid positions of the remaining connected components were used. The distance between cells was then determined by calculating the distance between the centers of mass of the nuclei. The mean number density, ρ_{N}, was calculated based on the number density of cells in each image. For MDCK cells and mouse skin, only cells within a radius of 20 μm from the center of the image were considered in the calculation of $N_{\mathrm{g}}(r)$ and ρ_{N}. In contrast, for intestinal organoids, all cells within the image were included in the calculation of $N_{\mathrm{g}}(r)$ and ρ_{N}.

The RDF for MDCK cells was calculated using 24 images for monolayers and 17 images for multilayers. For mouse skin, five images were analyzed for each stage. For intestinal cancer organoids, five images were analyzed for the control phenotype, and nine images were analyzed for the malignant phenotype.

3D modeling of epithelial stratification

We employed a 3D vertex model to calculate the dynamics of multiple cells comprising an epithelial sheet in 3D space. The dimensions of the system box were defined as $0 \leq x < L_x$, $0 \leq y < L_y$, with z extending infinitely in both directions ($-\infty < z < \infty$) in the xyz coordinates. We applied periodic boundary conditions at $x = 0$, L_x, $y = 0$, and L_y. Within this box, an epithelial sheet, consisting of N_{t} cells, was arranged in the xy plane.

Each cell within the epithelium was modeled as a polyhedron, with shared vertices between adjacent cells. Therefore, the shape and arrangement of cells in the epithelium were described by the positions of the vertices of the polyhedrons and the topological connections among these vertices. The epithelial polarity of each cell surface was defined based on this topology. The top and bottom surfaces of the sheet along the z axis were designated as the apical and basal surfaces, respectively, for each cell. Boundaries between adjacent cells were defined as lateral surfaces for each cell.

Cell movements are described by changes in the positions of the vertices. The time evolution of the position of the ith vertex, denoted by $\boldsymbol{r}_i$, is described by

$$\eta_i \left(\frac{d\boldsymbol{r}_i}{dt} - \boldsymbol{v}_i \right) = -\boldsymbol{\nabla}_i U \,. \tag{5}$$

The left-hand side of Eq. 5 represents the viscous force acting on the ith vertex. Here, η_i denotes the friction coefficient for this vertex, which is calculated as the sum of the friction coefficients from the adjacent cells, expressed as $\sum_{\alpha(i)}^{\text{cell}} \eta_c$, where η_c represents the friction coefficient between cells. The local velocity vector at the ith vertex, denoted by $\boldsymbol{v}_i$, in Eq. 5 is defined as the average velocity of the surrounding cells: $\sum_{\alpha(i)}^{\text{cell}} \boldsymbol{v}_\alpha \,/\, \sum_{\alpha(i)}^{\text{cell}}$, where $\boldsymbol{v}_\alpha$ is the velocity of the αth cell. $\boldsymbol{v}_\alpha$ is calculated as the average velocity of its constituent vertices. This formulation ensures the balance of the total viscous force within each cell.

During epithelial stratification, cell configurations were rearranged in 3D space. In our model, this cell rearrangement is described by introducing [H]-[I] operations[33]. When individual edges in the network occasionally shrink to meet or retract from neighboring cells, the topological network is reconnected. These [H]-[I] operations differ from the well-known T1 transformation commonly used in 2D vertex models but express several changes in 3D cell configurations, including the rearrangement of cells within the plane of the epithelium, stacking of cells vertically on the plane, and hole formation within the epithelial sheet.

Stress-free periodic boundary conditions

The right-hand side of Eq. 1 represents the mechanical force acting on the ith vertex, which is derived from the effective energy of the system, denoted by U. The effective energy U is the sum of the energies of individual cells, represented as $U = \sum_{\alpha}^{\text{cell}} u_\alpha$. Here, u_α denotes the effective energy of the αth cell, defined by

$$u_\alpha = \frac{K}{2}\left(\frac{V_\alpha}{V_0} - 1\right)^2 + \kappa A_\alpha + \Gamma (P_\alpha)^2 + \frac{\lambda}{2} P_\alpha \,. \tag{6}$$

In this equation, K, V_0, κ, Γ, and λ are constants, and $K, V_0, \kappa,$ and Γ are positive.

The first term of Eq. 6 represents the volume elastic energy, which serves to maintain the αth cell volume, denoted by V_α, to a preferable volume, V_0, with elasticity K. The second term in Eq. 2 represents the cortical surface energy, indicative of the basolateral surface tension κ, where A_α represents the total basolateral surface area of the αth cell. The third and fourth terms in Eq. 2 represent the line energy along the apical junction surrounding the αth cell apical perimeter. These terms express the effects of actomyosin-induced contractility and cadherin-mediated adhesion. Specifically, the third term, which is quadratic in the apical perimeter, P_α, reflects the contractility harmonized along the entire perimeter of each cell. Γ refers to the elasticity of the apical perimeter of the αth cell. In contrast,

the fourth term, linear in P_α, represents the tension exerted on each junction between adjacent cells, represented by λ.

During the simulation, we ensured that the axial stress in the xy plane was approximately free by affinely deforming the system box. This deformation is described by

$$\mu \frac{dL_i}{dt} = -\frac{V_\mathrm{t}}{L_i}\sigma_{ii}\,. \tag{7}$$

In this equation, the index i takes x and y, representing the respective axes. Here, V_t denotes the total volume of the cells, calculated as $V_\mathrm{t} = \sum_\alpha^{\mathrm{cell}} V_\alpha$. The constant μ is defined as the friction coefficient of the epithelial sheet to its surroundings. σ_{ii} represents the normal component of the stress tensor in the ith axis. The stress tensor of the system, denoted by σ_{ij}, is calculated by

$$\sigma_{ij} = \frac{\sum_\alpha^{\mathrm{cell}} \sigma_{ij}^\alpha V_\alpha}{V_\mathrm{t}}. \tag{8}$$

In this equation, σ_{ij}^α refers to the stress tensor of the αth cell. We define σ_{ij}^α by

$$\sigma_{ij}^\alpha = \frac{1}{V_\alpha}\sum_{\beta(\alpha)}^{\mathrm{vertex}} \left(\boldsymbol{r}_{\beta(\alpha)}\right)_j \left(\boldsymbol{f}_{\beta(\alpha)}\right)_i. \tag{9}$$

Here, $(\,)_i$ indicates the ith component of a vector. The vector $\boldsymbol{r}_{\beta(\alpha)}$ is the distance vector from the center of the αth cell to the position of the βth vertex. $\boldsymbol{f}_{\beta(\alpha)}$ represents the force acting on the βth vertex within the αth cell, given as $\boldsymbol{f}_{\beta(\alpha)} = -du_\alpha/d\boldsymbol{r}_\beta$.

Nondimensionalization and numerical simulations

Physical parameters were nondimensionalized by units: length, l, was scaled by $V_0^{1/3}$, time, τ, by $12.5\eta_\mathrm{c}/\kappa$, and energy, ε, by $50\kappa V_0^{2/3}$. We summarized all physical parameters used in the simulations in Table 1. For the numerical integration of Eq. 5, we employed the first order Euler's method with a time step of Δt, set to 0.005. Vertex velocities in Eq. 5 were iteratively solved by convergent calculations to ensure that the mean residual error was below the threshold, RE_th, set to 0.00001. Topological operations were applied to each edge and trigonal face when related edge lengths were under the threshold, Δl_th, set to 0.05, at each time interval of Δt_r, set to 1.0. Details of the numerical implementations are similar to those of our previous studies (34, 48, 49).

To determine the local energy minimum for each parameter set, we calculated the relaxation process of vertex positions using Eq. 5. The initial condition for these simulations was a disordered cell configuration within the monolayer. This condition was obtained by simulating tissue growth. This initial condition was created by proliferation from 100 cells to 401 cells under conditions that

maintained the monolayer. In the numerical simulations, five disordered monolayer sheets created with different seed values were used as initial conditions. Numerical simulation data were averaged using these five data sets.

Assessment of epithelial structures

The number of layers in the epithelium, N_{l}, is defined as

$$N_{\mathrm{l}} = \frac{2N_{\mathrm{t}}}{N_{\mathrm{a}} + N_{\mathrm{b}}}. \tag{10}$$

In Eq. 10, N_{a} is the number of cells with an apical surface, and N_{b} is the number of cells with a basal surface. N_{t} is the number of total cells. This formula applies the trapezoidal formula and measures the average tissue height. This value represents the average number of layers in the tissue.

The nucleation ratio, f_{n}, and the growth ratio, f_{g}, are defined as

$$f_{\mathrm{n}} = \frac{N_{\mathrm{n}}}{N_{\mathrm{t}}}, \quad f_{\mathrm{g}} = \frac{N_{\mathrm{g}}}{N_{\mathrm{t}}}, \tag{11}$$

respectively. In Eq. 11, N_{n} represents the number of cells delaminated through the nucleation process, N_{g} represents the number of cells delaminated through the growth process, and N_{t} represents the total number of cells, including those that were not delaminated.

The planar cell density, ρ, is defined as

$$\rho = \langle \frac{2}{A_{\alpha}^{a} + A_{\alpha}^{b}} \rangle. \tag{12}$$

In Eq. 12, A_{α}^{a} and A_{α}^{b} represent the apical and basal surface areas of the α-th cell, respectively, and the symbol $\langle\ \rangle$ denotes the average value.

The apical junctional tension was calculated using Eq. 3. For an arbitrary apical junctional edge with length l, the average apical junctional tension, F_{jct}, was determined by $F_{\mathrm{jct}} = \langle\ \partial U/\partial l \rangle$. Upon calculation, F_{jct} was given by

$$F_{\mathrm{jct}} = \langle\ 2\Gamma P_{\alpha} + \lambda \rangle. \tag{13}$$

Theoretical model of 3D foam geometry and mechanics

A theoretical model was developed to analyze single-cell delamination, as previously described[30]. For simplification, we assumed that the apical and basal surfaces were constrained in the plane and considered only the movements of a single center cell and its first neighbors within the sheet while keeping the other neighboring cells fixed in position. Under this approximation, the in-plane cell density ρ implicitly reflects mechanical effects of the surrounding cells.

We modeled the center cell as an n-sided regular frustum ($n \geq 3$) with volume V, apical surface area A_{a}, and basal surface area A_{b}. The set of n, V, A_{a}, and A_{b} uniquely determines the shape of the center cell. In this geometry, the center cell has an apical surface, a basal surface, or both and is adjacent to n first-neighbor cells with which it shares lateral boundary faces. The n first-neighbor cells also share lateral boundary faces and are aligned radially around the center cell. Additionally, we introduced several geometric parameters, including the height of the center cell H, apical perimeter of the center cell P_{c} (≥ 0), total area of the n boundary faces between the center cell and its first-neighbor cells A_{c} (≥ 0), and total area of the n boundary faces between the first-neighbor cells A_{p}.

To describe the local deformation of the cell, we introduced the cell taper as defined by

$$d = \frac{\sqrt{A_{\mathrm{a}}} - \sqrt{A_b}}{\sqrt{A_{\mathrm{a}}} + \sqrt{A_b}}. \tag{14}$$

We modeled the mechanical energy of the epithelial sheet as follows. First, we assumed a fixed volume for each cell because the cell volume is almost constant during morphological changes in several organisms. Even under the constraints of constant cell volume and planar geometry, the cell-cell boundaries can move in principle, so d remained variable. To consider the same situation as a numerical simulation, we introduced the same energy function described in Eq. 3.

The first term in Eq. 3 is negligible because the total volume of each cell is assumed to be constant. However, the other terms are effective, because only the vertices constituting the center cell can move. We expanded the second term around the center cell and first-neighbor cells as $\kappa(A_{\mathrm{c}} + A_{\mathrm{p}})$. Similarly, we expanded the third term as $\Gamma\{1 + (1/n)[1 - \csc(\pi/n)]\}$, where $\{1 + (1/n)[1 - \csc(\pi/n)]\}$ is a correction factor that reflects the effects of the center cell and first-neighbor cells. Finally, we expanded the last term as $\lambda[2 - \csc(\pi/n)]$, where $[2 - \csc(\pi/n)]$ is a correction factor that reflects the effects of the center cell and first-neighbor cells. Thus, Eq. 3 can be written as the mechanical energy of the center cell and first-neighbor cells in the planar sheet as described by

$$\begin{aligned} U_{\mathrm{p}} = \kappa(A_c + A_p) + \Gamma\left[1 + \frac{1}{n}\left(1 - \csc\left(\frac{\pi}{n}\right)\right)^2\right](P_{\mathrm{c}} - P_{\mathrm{eq}})^2 \\ + \lambda\left[2 - \csc\left(\frac{\pi}{n}\right)\right](P_{\mathrm{c}} - P_{\mathrm{eq}}). \end{aligned} \tag{15}$$

The packing geometry imposes geometric constraints on the physical parameters. We simultaneously solved Eq. 15 and obtained H, A_{a}, and A_{b} as functions of ρ, V, and d as described by

$$H(\rho, V) = \rho V \tag{16}$$

$$A_{\mathrm{a}}(\rho, d) = \frac{3(d+1)^2}{\rho(d^2+3)} \tag{17}$$

$$A_{\mathrm{b}}(\rho, d) = \frac{3(d-1)^2}{\rho(d^2+3)} \tag{18}$$

The geometric parameters P_{c}, A_{c}, and A_{p} in the energy function U are described as functions of n, H, A_{a}, and A_{b} as described by

$$P_{\mathrm{c}}(n, A_{\mathrm{a}}) = 2\sqrt{nA_{\mathrm{a}}\tan\left(\frac{\pi}{n}\right)} \tag{19}$$

$$A_{\mathrm{c}}(n, H, A_{\mathrm{a}}, A_{\mathrm{b}}) = \left(\sqrt{A_{\mathrm{a}}} + \sqrt{A_{\mathrm{b}}}\right)\sqrt{A_{\mathrm{a}} - 2\sqrt{A_{\mathrm{a}}A_{\mathrm{b}}} + A_{\mathrm{b}} + H^2\tan\left(\frac{\pi}{n}\right)} \tag{20}$$

$$A_{\mathrm{p}}(n, H, A_{\mathrm{a}}, A_{\mathrm{b}}) = C - H\sqrt{\frac{n}{2\sin\left(\frac{2\pi}{n}\right)}}\left(\sqrt{A_{\mathrm{a}}} + \sqrt{A_{\mathrm{b}}}\right) \tag{21}$$

Where C is a constant that represents the total area of the boundary faces between neighbor cells and the cross section in the center cell. Because A_{p} is incorporated into the energy function in Eq. 3 as a first-order process, C is negligible. Using the analytical expressions of U_{p}, we then calculated energy landscapes as functions of d under specific n, ρ, and λ values.

AFM measurement of cell stiffness

For the AFM measurements, we used a JPK Nanowizard 4 (Bruker) equipped as a confocal microscope (Expert line, Abberior). To measure stiffness at cell-cell junctions, we used a 3XC-GG cantilever (OPUS, spring constant 0.1–0.6 N/m). Immediately before measurement, the medium was replaced with DMEM supplemented with 10% serum, 1% penicillin/streptomycin, and 10 mM HEPES. The following parameters were set: setpoint of 2–4 nN, *z* length of 6–8 μm, *z* speed of 100–120 μm/s, and a scan area of either 30 × 30 or 50 × 50 μm with a resolution of 128 × 128 or 256 × 256 pixels. After measurement, fluorescence images were captured using confocal microscopy, similar to the epithelial measurement. After averaging and baseline subtraction, Young's modulus was calculated using a Hertz model with a triangular pyramid half-cone angle of 35°. The Young's modulus map was then exported and converted to monochrome. Cell-cell junction regions were manually extracted from these maps, and the junctional stiffness at each pixel was obtained using Gwyddion software.

After each AFM measurement, 3D fluorescence images were acquired using a confocal microscope (Expert Line, Abberior) with a 60× lens (NA 0.7). Images were acquired with 560 nm illumination, 10% laser power, and a 10-μs exposure time per pixel. The scan size was 120 × 120 μm with a resolution of 600 × 600 pixels in the *xy* plane and 20–25 μm in the *z* axis with a 1 μm interval. To assess the dependence of epithelial stiffness, the planar cell density was calculated from the 3D fluorescence images. Because the AFM scan area was centered in the fluorescence image, the image

was cropped to a size of 60 × 60 μm including the AFM scan area. A total of 19 stiffness maps were obtained from four dishes.

Materials and Data Availability

All materials and data supporting the findings of this study are available from the corresponding author upon reasonable request.

References

1. Gilbert, S. F. *Developmental Biology*. (Sinauer associates Sunderland, MA, 2016).
2. Ya-Xian, Z., Suetake, T. & Tagami, H. Number of cell layers of the stratum corneum in normal skin – relationship to the anatomical location on the body, age, sex and physical parameters. *Arch Dermatol Res* **291**, 555–559 (1999).
3. Morita, R. *et al.* Tracing the origin of hair follicle stem cells. *Nature* **594**, 547–552 (2021).
4. Masterton, S. & Ahearne, M. Mechanobiology of the corneal epithelium. *Experimental Eye Research* vol. 177 122–129 Preprint at https://doi.org/10.1016/j.exer.2018.08.001 (2018).
5. Zhang, Y., Bailey, D., Yang, P., Kim, E. & Que, J. The development and stem cells of the esophagus. *Development (Cambridge)* vol. 148 Preprint at https://doi.org/10.1242/dev.193839 (2021).
6. Arellano, J., Storch, V. & Sarasquete, C. Histological and histochemical observations in the stomach of the Senegal sole, Solea senegalensis. *Histol Histopathol* **16**, 511–521 (2001).
7. Moxey, P. C. & Trier, J. S. Specialized cell types in the human fetal small intestine. *Anat Rec* **191**, 269–285 (1978).
8. Ehrhardt, C. *et al. 16HBE14o-Human Bronchial Epithelial Cell Layers Express P-Glycoprotein, Lung Resistance-Related Protein, and Caveolin-1*. (2003).
9. Tosches, M. A. *et al.* Evolution of pallium, hippocampus, and cortical cell types revealed by single-cell transcriptomics in reptiles. *Science (1979)* **360**, 881–888 (2018).
10. Mills, A. A. *et al.* p63 is a p53 homologue required for limb and epidermal morphogenesis. *Nature* **398**, 708–713 (1999).
11. Koster, M. I., Kim, S., Mills, A. A., DeMayo, F. J. & Roop, D. R. p63 is the molecular switch for initiation of an epithelial stratification program. *Genes Dev* **18**, 126–131 (2004).
12. Romano, R. A. *et al.* ΔNp63 knockout mice reveal its indispensable role as a master regulator of epithelial development and differentiation. *Development* **139**, 772–782 (2012).
13. Fiore, V. F. *et al.* Mechanics of a multilayer epithelium instruct tumour architecture and function. *Nature* **585**, 433–439 (2020).
14. Nakajima, Y. I., Meyer, E. J., Kroesen, A., McKinney, S. A. & Gibson, M. C. Epithelial junctions maintain tissue architecture by directing planar spindle orientation. *Nature* **500**, 359–362 (2013).
15. Damen, M. *et al.* High proliferation and delamination during skin epidermal stratification. *Nat Commun* **12**, (2021).
16. Huebner, R. J., Lechler, T. & Ewald, A. J. Developmental stratification of the mammary epithelium occurs through symmetry-breaking vertical divisions of apically positioned luminal cells. *Development (Cambridge)* **141**, 1085–1094 (2014).
17. Packard, A. *et al.* Luminal Mitosis Drives Epithelial Cell Dispersal within the Branching Ureteric Bud. *Dev Cell* **27**, 319–330 (2013).
18. Fujita, I. *et al.* Endfoot regeneration restricts radial glial state and prevents translocation into the outer subventricular zone in early mammalian brain development. *Nat Cell Biol* **22**, 26–37 (2020).
19. Vaezi, A., Bauer, C., Vasioukhin, V. & Fuchs, E. *Actin Cable Dynamics and Rho/Rock Orchestrate a Polarized Cytoskeletal Architecture in the Early Steps of Assembling a Stratified Epithelium Integrin Superfamily, Whereas Cell-Cell Contacts Are Me-Diated by Homotypic Interactions of the Transmembrane Family of Cadherins. Biochemical and Gene-Targeting Studies Indicate That Both Types of Junctions Participate in Establishing a Polarized Epidermal Architecture (Hodi*. *Developmental Cell* vol. 3 http://www.developmentalcell. (2002).
20. Simpson, C. L., Patel, D. M. & Green, K. J. Deconstructing the skin: cytoarchitectural determinants of epidermal morphogenesis. *Nat Rev Mol Cell Biol* **12**, 565–580 (2011).

21. Takagi, M. *et al.* Accumulation of the myosin-II-spectrin complex plays a positive role in apical extrusion of Src-transformed epithelial cells. *Genes to Cells* **23**, 974–981 (2018).
22. Dias Gomes, M., Letzian, S., Saynisch, M. & Iden, S. Polarity signaling ensures epidermal homeostasis by coupling cellular mechanics and genomic integrity. *Nat Commun* **10**, (2019).
23. Teo, J. L. *et al.* Caveolae Control Contractile Tension for Epithelia to Eliminate Tumor Cells. *Dev Cell* **54**, 75-91.e7 (2020).
24. Vincent, J.-P., Fletcher, A. G. & Baena-Lopez, L. Al. Mechanisms and mechanics of cell competition in epithelia. *Nat Rev Mol Cell Biol* **14**, 581–591 (2013).
25. Marinari, E. *et al.* Live-cell delamination counterbalances epithelial growth to limit tissue overcrowding. *Nature* **484**, 542–545 (2012).
26. Levayer, R., Dupont, C. & Moreno, E. Tissue Crowding Induces Caspase-Dependent Competition for Space. *Current Biology* **26**, 670–677 (2016).
27. Eisenhoffer, G. T. *et al.* Crowding induces live cell extrusion to maintain homeostatic cell numbers in epithelia. *Nature* **484**, 546–549 (2012).
28. Saw, T. B. *et al.* Topological defects in epithelia govern cell death and extrusion. *Nature* **544**, 212–216 (2017).
29. Box, K., Joyce, B. W. & Devenport, D. Epithelial geometry regulates spindle orientation and progenitor fate during formation of the mammalian epidermis. *Elife* **8**, e47102 (2019).
30. Okuda, S. & Fujimoto, K. A Mechanical Instability in Planar Epithelial Monolayers Leads to Cell Extrusion. *Biophys J* **118**, 2549–2560 (2020).
31. Guillamat, P., Blanch-Mercader, C., Pernollet, G., Kruse, K. & Roux, A. Integer topological defects organize stresses driving tissue morphogenesis. *Nat Mater* **21**, 588–597 (2022).
32. Sarkar, T. *et al.* Crisscross multilayering of cell sheets. *PNAS Nexus* **2**, (2023).
33. Okuda, S., Inoue, Y., Eiraku, M., Sasai, Y. & Adachi, T. Reversible network reconnection model for simulating large deformation in dynamic tissue morphogenesis. *Biomech Model Mechanobiol* **12**, 627–644 (2013).
34. Hashimoto, A., Nagao, A. & Okuda, S. Topological graph description of multicellular dynamics based on vertex model. *J Theor Biol* **437**, 187–201 (2018).
35. Kajita, M. *et al.* Interaction with surrounding normal epithelial cells influences signalling pathways and behaviour of Src-transformed cells. *J Cell Sci* **123**, 171–180 (2010).
36. Moitrier, S. *et al.* Local light-activation of the Src oncoprotein in an epithelial monolayer promotes collective extrusion. *Commun Phys* **2**, 98 (2019).
37. Kajiwara, K. *et al.* Src activation in lipid rafts confers epithelial cells with invasive potential to escape from apical extrusion during cell competition. *Current Biology* **32**, 3460-3476.e6 (2022).
38. Fanfoni, M. & Tomellini, M. The Johnson-Mehl-Avrami-Kolmogorov model: A brief review (*). 7–8 (1998).
39. Galle, J., Loeffler, M. & Drasdo, D. Modeling the effect of deregulated proliferation and apoptosis on the growth dynamics of epithelial cell populations in vitro. *Biophys J* **88**, 62–75 (2005).
40. Kobayashi, Y., Sawabu, Y., Kitahata, H., Denda, M. & Nagayama, M. Mathematical model for calcium-assisted epidermal homeostasis. *J Theor Biol* **397**, 52–60 (2016).
41. Du, H. *et al.* Multiscale modeling of layer formation in epidermis. *PLoS Comput Biol* **14**, (2018).
42. Farhadifar, R., Röper, J. C., Aigouy, B., Eaton, S. & Jülicher, F. The Influence of Cell Mechanics, Cell-Cell Interactions, and Proliferation on Epithelial Packing. *Current Biology* **17**, 2095–2104 (2007).
43. Okuda, S., Unoki, K., Eiraku, M. & Tsubota, K. I. Contractile actin belt and mesh structures provide the opposite dependence of epithelial stiffness on the spontaneous curvature of constituent cells. *Dev Growth Differ* **59**, 455–464 (2017).
44. Okuda, S. *et al.* Strain-triggered mechanical feedback in self-organizing optic-cup morphogenesis. *Sci Adv* **4**, eaau1354 (2018).

45. Okuda, S., Kuranaga, E. & Sato, K. Apical Junctional Fluctuations Lead to Cell Flow while Maintaining Epithelial Integrity. *Biophys J* **116**, 1159–1170 (2019).
46. Bi, D., Yang, X., Marchetti, M. C. & Manning, M. L. Motility-Driven Glass and Jamming Transitions in Biological Tissues. *Phys Rev X* **6**, 21011 (2016).
47. Ito, S. *et al.* Induced cortical tension restores functional junctions in adhesion-defective carcinoma cells. *Nat Commun* **8**, 1834 (2017).
48. Gómez-Gálvez, P. *et al.* Scutoids are a geometrical solution to three-dimensional packing of epithelia. *Nat Commun* **9**, 2960 (2018).
49. Richardson, R. J. *et al.* Periderm prevents pathological epithelial adhesions during embryogenesis. *Journal of Clinical Investigation* **124**, 3891–3900 (2014).
50. Hu, M. S. *et al.* Embryonic skin development and repair. *Organogenesis* vol. 14 46–63 Preprint at https://doi.org/10.1080/15476278.2017.1421882 (2018).
51. Sakai, E. *et al.* Combined mutation of Apc, Kras, and Tgfbr2 effectively drives metastasis of intestinal cancer. *Cancer Res* **78**, 1334–1346 (2018).
52. Wang, D. *et al.* Nano-scale physical properties characteristic to metastatic intestinal cancer cells identified by high-speed scanning ion conductance microscope. *Biomaterials* **280**, (2022).
53. Tunggal, J. A. *et al.* E-cadherin is essential for in vivo epidermal barrier function by regulating tight junctions. *EMBO J* **24**, 1146-1156–1156 (2005).
54. Lubkov, V. & Bar-Sagi, D. E-Cadherin-Mediated Cell Coupling Is Required for Apoptotic Cell Extrusion. *Current Biology* **24**, 868–874 (2014).
55. Wu, S. K., Lagendijk, A. K., Hogan, B. M., Gomez, G. A. & Yap, A. S. Active contractility at E-cadherin junctions and its implications for cell extrusion in cancer. *Cell Cycle* **14**, 315–322 (2015).
56. Alexander A. Chernov. Modern crystallography. III. *J Appl Crystallogr* **17**, 488 (1984).
57. Avery's Diseases of the Newborn. in *Avery's Diseases of the Newborn (Tenth Edition)* (Elsevier, Philadelphia, 2018). doi:https://doi.org/10.1016/B978-0-323-40139-5.00111-X.
58. Mishima, O., Calvert, L. D. & Whalley, E. An apparently first-order transition between two amorphous phases of ice induced by pressure. *Nature* **314**, 76–78 (1985).
59. Durandurdu, M. & Drabold, D. A. Ab initio simulation of first-order amorphous-to-amorphous phase transition of silicon. *Phys Rev B* **64**, 14101 (2001).
60. Wang, Y.-C. *et al.* In situ TEM study of deformation-induced crystalline-to-amorphous transition in silicon. *NPG Asia Mater* **8**, e291–e291 (2016).
61. Huang, L. & Kieffer, J. Amorphous-amorphous transitions in silica glass. I. Reversible transitions and thermomechanical anomalies. *Phys Rev B* **69**, 224203 (2004).
62. Guerette, M., Ackerson, M. R., Thomas, J., Watson, E. B. & Huang, L. Thermally induced amorphous to amorphous transition in hot-compressed silica glass. *J Chem Phys* **148**, 194501 (2018).
63. Miroshnikova, Y. A. *et al.* Adhesion forces and cortical tension couple cell proliferation and differentiation to drive epidermal stratification. *Nat Cell Biol* **20**, 69–80 (2018).
64. Priya, R. *et al.* Tension heterogeneity directs form and fate to pattern the myocardial wall. *Nature* **588**, 130–134 (2020).
65. Liu, X., Cleary, J. & German, G. K. The global mechanical properties and multi-scale failure mechanics of heterogeneous human stratum corneum. *Acta Biomater* **43**, 78–87 (2016).
66. Sato, T. *et al.* Single Lgr5 stem cells build crypt-villus structures in vitro without a mesenchymal niche. *Nature* **459**, 262–265 (2009).
67. Matsumoto, K. *et al.* Advanced CUBIC tissue clearing for whole-organ cell profiling. *Nat Protoc* **14**, 3506–3537 (2019).